Magnetic and magnetocaloric properties of HoCrO_{3} tuned by selective rare-earth doping

Shiqi Yin, Mohindar S. Seehra, Curtis J. Guild, Steven L. Suib, Narayan Poudel, Bernd Lorenz, and Menka Jain

Phys. Rev. B **95**, 184421 — Published 18 May 2017

DOI: 10.1103/PhysRevB.95.184421

Magnetic and magneto-caloric properties of $HoCrO_3$ tuned by selective rare-earth doping

Shiqi Yin,[1] Mohindar. S. Seehra,[2] Curtis J. Guild,[3] Steven L. Suib,[3,4] Narayan Poudel,[5] Bernd Lorenz,[5] and Menka Jain [1,4,*]

[1] *Department of Physics, University of Connecticut, Storrs, Connecticut 06269, USA*

[2] *Department of Physics and Astronomy, West Virginia University, Morgantown, West Virginia 26506, USA*

[3] *Department of Chemistry, University of Connecticut, Storrs, Connecticut 06269, USA*

[4] *Institute of Materials Science, University of Connecticut, Storrs, Connecticut 06269, USA*

[5] *Texas Center for Superconductivity and Department of Physics, University of Houston, Houston, Texas 77204, USA*

Abstract

Rare-earth chromites ($RCrO_3$) are an important sub-class of functional materials with interesting magnetic, electrical, and catalytic properties that make them promising for various applications. Here, we report comparisons on the structural and magnetic properties of $HoCrO_3$ with those of $Ho_{0.67}Tm_{0.33}CrO_3$ and $Ho_{0.67}Gd_{0.33}CrO_3$ powder samples, which were doped by Tm^{3+} (or Gd^{3+}) ions at the A-site with ionic radius smaller (or larger) than that of Ho^{3+} ion. The structural properties of the samples were characterized by X-ray diffraction, Raman spectroscopy, and scanning electron microscopy carried out at ambient. The band gaps of the three samples were determined by analyzing their UV-Vis spectra. Magnetic studies carried out from 5K to 300 K in magnetic fields up to 70 kOe show that the Néel temperature (T_N^{Cr}, where Cr^{3+} ions order) increases with an increase in the average A-site (R-site) ionic radius, tolerance factor, and Cr1-O1-Cr1 bond angle, but decreases with an increase in the orthorhombic strain factor. In addition, the application of external hydrostatic pressure was found to enhance T_N^{Cr} of $HoCrO_3$, similar to the effect observed by doping $HoCrO_3$ with Gd^{3+} ions. These changes in T_N^{Cr} with A-site doping and hydrostatic pressure are related to changes in Cr^{3+}-Cr^{3+} exchange coupling resulting from changes in the Cr1-O1-Cr1 bond angle and Cr1-O1 bond lengths respectively. Temperature dependent paramagnetic susceptibility data of the samples was fitted to the modified Curie-Weiss law that included the Dzyloshinskii-Moriya interaction. Isothermal magnetization data showed that the magnetic behavior of the samples changes from canted antiferromagnetism at low temperatures to paramagnetism at higher temperatures. The large magneto-caloric entropy change was observed in $HoCrO_3$ which was enhanced by Gd doping but lowered by Tm doping showing its tunability by A-site doping. Correlation between magneto-electric properties and magnetization is discussed.

* Author to whom correspondence should be addressed. Electronic mail: menka.jain@uconn.edu

1. Introduction

Materials with more than one ferroic orders: ferroelectricity (FE), ferromagnetism (FM), and ferro-elasticity are known as multiferroics [1-4]. Among the multiferroics, rare-earth chromites ($RCrO_3$, R=Ho, Er, Yb, Lu, and Y) are a type of magneto-electric multiferroics with coexistence of FE and magnetic orders [5-8]. These $RCrO_3$ exhibit canted antiferromagnetism below the Néel temperatures (T_N=113–140 K depending on R ion); while their FE transition temperatures (T_C) and associated mechanisms are still debated [5,9,10]. For example, Sahu *et al.* invoked the Curie-Weiss law by plotting the reciprocal of dielectric constant in the high-temperature region versus temperature data, and the T_C values were determined to be in the 472–516 K range for $HoCrO_3$, $ErCrO_3$, $YbCrO_3$, and $LuCrO_3$, independent of frequency [5]. However, Ghosh *et al.* reported a much lower T_C of 240 K for both $HoCrO_3$ bulk and thin films [11]. Similarly, the T_C of $SmCrO_3$ was reported to be 220 K, somewhat higher than its T_N=193 K [12]. For $YCr_{0.5}Fe_{0.5}O_3$ samples, Rajeswaran *et al.* have reported T_C and T_N to be nearly equal at 260 K [10].

Semiconducting nature of the $RCrO_3$ compounds has also attracted attention for photo-catalytic and other light-harvesting applications [13-16]. Gupta *et al.* measured the UV-Vis absorption spectra and explored the photocatalytic activity of $DyCrO_3$ nano-platelets [13]. Some doped $RCrO_3$ compounds have also been investigated for hydrocarbon oxidation [17]. Compared to conventional photocatalytic materials like TiO_2, $RCrO_3$ has advantages of strong absorption bands in the visible frequency range [18]. Doped $LaCrO_3$ perovskites are utilized in solid-oxide fuel cells due to their excellent energy conversion efficiency and high fuel flexibility resulting from the high operation temperatures [19,20]. In general, $RCrO_3$ compounds are *p*-type semiconductors with electronic sensitivity to humidity and gases (H_2, NO, N_2O, etc.), which makes them useful for sensor applications [21,22]. In addition, large magneto-caloric effects (MCE) observed at temperatures below 30 K renders some $RCrO_3$ compounds useful for applications in low-temperature magnetic refrigeration [16,23-26].

Various interesting properties of the $RCrO_3$ compounds with orthorhombically distorted perovskite (ABO_3) structure stems from strong correlations among their structural, electric, and magnetic properties [27]. In general, the perovskite structure can accommodate host ions with a range of ionic radii, which makes chemical substitution/doping an effective way to tune their structural and magnetic properties. For example, Sharma *et al.* reported that Dy and Ho doping at the Tb-site in $TbMnO_3$ increase Mn-O-Mn bond angles and induce weak ferromagnetism at 60 K and 63 K, respectively [28]. With iso-structure as $TbMnO_3$, $RCrO_3$ compounds contain corner-shared CrO_6 octahedra with the Cr^{3+} ions in the center and R^{3+} ions occupying vacant sites between the CrO_6 octahedral sites. The mismatch between R-O and Cr-O bond lengths in the Goldsmidt tolerance factor ($t = (r_{R^{3+}} + r_{O^{2-}})/\sqrt{2}(r_{Cr^{3+}} + r_{O^{2-}}) < 1$) leads to considerable

cooperative rotations of the CrO_6 octahedra, which decreases with increasing R^{3+} ionic radius. With rare-earth dopants on the A-site (i.e. R-site), Cr1-O1-Cr1 bond angles in $RCrO_3$ is expected to change like those in orthorhombic $RMnO_3$ [28,29]. Therefore, it would be interesting to study the dependence of the structural and magnetic properties of $RCrO_3$ with chemical doping (chemical pressure) and/or applying external hydrostatic pressure. Recently, Fe doping at the Cr-site of $DyCrO_3$ and $HoCrO_3$ was found to enhance their respective T_N and affect their magneto-caloric properties at low temperatures [16,24]. McDannald *et al*. also reported that Ho and Y doping on the A-site lowers the MCE (magneto-caloric effect) of $DyCrO_3$ powder samples, while Er doping improves the MCE [25]. It should be noted that the application of external pressure in compounds with distorted perovskite structures is an alternate approach to modify structural distortions as reported for $DyMnO_3$ [30], and $RCrO_3$ [31], along with the theoretical reports on structural distortions in $RFeO_3$ [32] and structural/magnetization behavior in $RCrO_3$ [33] recently. However, experimental investigations on the effect of pressure on magnetic properties of $RCrO_3$ is still lacking.

To our knowledge, the effects of chemical pressure (i.e. by doping at the A-site) of $HoCrO_3$ on its structural, optical, and magnetic properties and effect of hydrostatic pressure on it magnetic property have not been reported yet. Hence, our aim in the present study is to experimentally explore the effect of A-site doping on the structural and magnetic properties of $HoCrO_3$ bulk samples with an emphasis on the changes of their MCE properties. To explore both ends of the induced chemical pressure, we chose to substitute the A-site in $HoCrO_3$ with two rare-earth ions: Tm^{3+} and Gd^{3+}, which have smaller and larger ionic radius than that of Ho^{3+}, respectively. The compositions that are studied here are $Ho_{0.67}Tm_{0.33}CrO_3$, $HoCrO_3$, and $Ho_{0.67}Gd_{0.33}CrO_3$. In addition, the effect of hydrostatic pressure on the magnetic properties of bulk $HoCrO_3$ sample is also reported. It was found that the A-site doping with a larger ion (than Ho^{3+}) had similar effect as the application of external hydrostatic pressure on the magnetic properties of $HoCrO_3$.

2. Experimental Procedures

To prepare $Ho_{0.67}Tm_{0.33}CrO_3$ (HTCO), $HoCrO_3$ (HCO), and $Ho_{0.67}Gd_{0.33}CrO_3$ (HGCO) powder samples, first $Ho(NO_3)_3$, $Tm(NO_3)_3$, $Gd(NO_3)_3$, and $Cr(NO_3)_3$ precursors (99.999% purity) were dissolved in water in stoichiometric ratios and then mixed in a beaker using magnetic stirrer on a hot plate. Then, after the addition of citric acid, the three solutions were dried and the resultant powders were annealed at 900 °C in oxygen environment for 2 hours each. The structure and phase purity of the samples were investigated by room-temperature X-ray diffraction (XRD) (Bruker D2) and Raman spectroscopy (Renishaw System 2000). Scanning electron microscopy (SEM) images were obtained using a JEOL JSM-6335F instrument. Energy-dispersive X-ray spectroscopy (EDS) was recorded to verify the chemical composition by an

energy dispersive spectrometer attached to an FEI Teneo LVSEM. Optical absorbance was measured with a diffuse reflectance integrating sphere attached to a Shimadzu UV-2450 UV-Vis Spectrometer. The UV-Vis measurements were performed by dispersing the sample in barium sulfate, which was also used as a reflective reference. The dc and ac magnetization measurements were performed by vibrating sample magnetometer and ac magnetic system attached to the Evercool physical property measurement system (PPMS from Quantum Design), respectively. For the hydrostatic pressure measurements, first the powder samples were mixed with polyvinyl alcohol (PVA) solution as the binder and dried. The resultant powder was then compressed into a pellet with a dye, followed by annealing at 1300 °C for 4 hours in air. A small piece of the pellet was cut and wound with insulated copper wire. After two layers of thinner wire (secondary coil) were wound on the top of it, two layers of thicker wire (primary coil) were wound. The sample and thermocouple was placed inside a Teflon tube where the contact wires were taken out from the copper cap. The Teflon tube with sample was inserted into a Be-Cu cylinder supplied with two pistons on the top and bottom. The cylinder was inserted into the pressure cell and pressure was applied with a hydraulic press [34]. The pressure cell was screwed to the probe and inserted into a wide mouth Dewar filled with liquid nitrogen. The temperature was controlled by lowering or raising the probe in the Dewar, and measured using a chromel/alumel thermocouple. The rate of cooling and warming rate ranged from 1 K to 3 K per minute. The sample pressure was estimated from the calibration curve of the pressure cell. The excitation current was driven in the primary coil and the mutual inductance signal in the secondary coil was measured with a 19 Hz, LR 700 AC resistance-bridge. When the magnetic properties of the sample changes, an anomaly in the mutual inductance of secondary coil is observed.

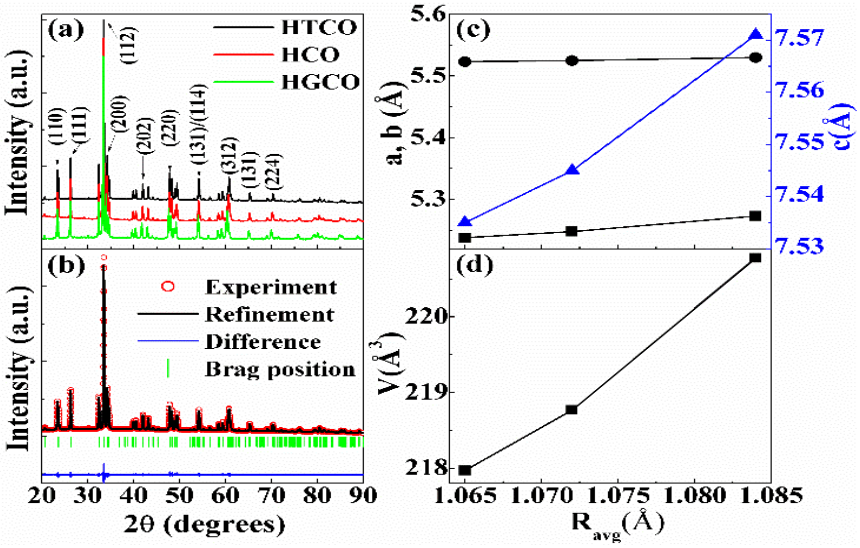

FIG. 1. (a) X-ray diffraction data of $Ho_{0.67}Tm_{0.33}CrO_3$ (HTCO), $HoCrO_3$ (HCO), and $Ho_{0.67}Gd_{0.33}CrO_3$ (HGCO) samples; (b) Representative X-ray diffraction data and Rietveld refinement results of HTCO; A-site ionic radius (R_{avg}) dependence of the lattice parameters *a* (squares), *b* (circles), and *c* (triangles) is shown in (c) and that of the volume of the unit cell (V) in (d) with the lines connecting the data points as visual guides.

3. Results and discussion

3.1. Structural characteristics

Fig. 1(a) shows the XRD patterns of the present samples. All the major peaks for each sample could be indexed based on an ortho-rhombically distorted perovskite structure with space group *Pbnm*. Thus, these samples were determined to be phase pure within the detection limit of laboratory XRD. Rietveld refinement was used to analyze the XRD data for each composition. A representative Rietveld refined pattern of HTCO sample is shown in Fig. 1(b). The lattice parameters *a*, *b*, and *c* of the present samples obtained from the Rietveld refinement are listed in Table I and these agree well with the reported values for $HoCrO_3$, $TmCrO_3$, and $GdCrO_3$ [35]. It was found that (and as shown in the Figure 1(c)) the lattice parameters of $HoCrO_3$ decrease with Tm doping and increase with Gd doping. This difference could be interpreted by the effect of dopant on the average A-site ionic radius $R_{avg} = \sqrt{0.33 * R_{Tm/Gd}^2 + 0.67 * R_{Ho}^2}$ for HTCO and HGCO samples. Here R_{Tm}, R_{Ho}, and R_{Gd} are 1.052 Å, 1.072 Å, and 1.107 Å, respectively. As shown in Figs. 1(c) and 1(d), the lattice parameters *a*, *b*, *c*, and cell volume (V) increase with increase in R_{avg}, which matches well with the experimental [35,36] and computational work [33]. From Rietveld refinement, the in-plane Cr1-O1-Cr1 bond angle, Cr1-O1 bond length, and atomic positions were also determined (see Table I). Note that the in-plane Cr1-O1-Cr1 bond angle increases with increasing R_{avg} in agreement with the computational results [33].

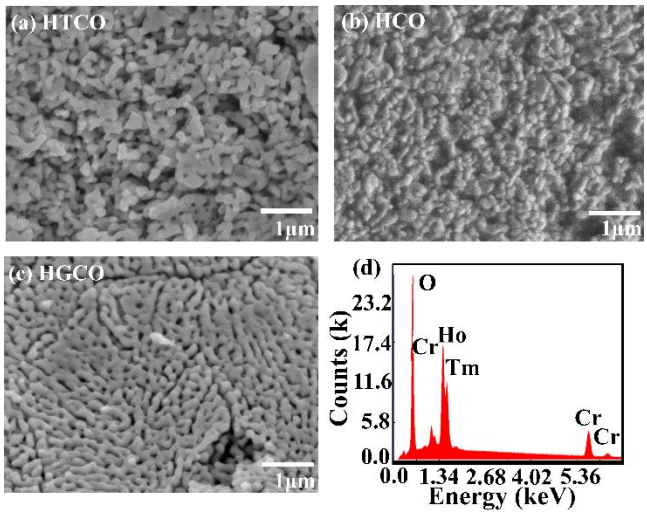

FIG. 2. Scanning electron microscopy images of (a) $Ho_{0.67}Tm_{0.33}CrO_3$ (HTCO), (b) $HoCrO_3$ (HCO), and (c) $Ho_{0.67}Gd_{0.33}CrO_3$ (HGCO) samples. (d) Energy-dispersive X-ray spectroscopy of HTCO sample shows the presence of Ho, Tm, Cr, and O elements.

Table I also summarizes the value of the afore-mentioned Goldsmidt tolerance factor (t), and the orthorhombic distortions (S) of the unit cells from the cubic structure characterized by $S= 2(b-a) / (b+a)$. With increasing R_{avg}, t increases but S decreases. The crystallite size L of the powder samples were estimated using the Scherrer equation: $L = K \lambda /(\beta \cos\theta)$ [37, 38]. Here β is the full width at half maximum (FWHM) of a diffraction peak in radians after subtracting the instrumental line broadening, θ is the Bragg angle, $K \approx 0.89$ is a dimensionless shape factor and λ is the X-ray wavelength. Using the Fityk software [39], β was obtained by Pearson 7 peak fitting of the (hkl) peaks in the XRD data. The values of L of the present samples, calculated to be around 100 nm, are listed in Table 1.

Table 1. Lattice parameters, average A-site ionic radius (R_{avg}), Goldsmidt tolerance factor (t), orthorhombic strain (S), Cr1-O1-Cr1 bond angles, Cr1-O1 bond length, and atomic positions obtained from Rietveld refinement of the experimental XRD data, along with the average crystallite size (L) calculated by Scherrer equation for the present samples.

Sample	**$Ho_{0.67}Tm_{0.33}CrO_3$**	**$HoCrO_3$**	**$Ho_{0.67}Gd_{0.33}CrO_3$**
a(Å)	5.23794(3)	5.24825(5)	5.27317(7)
b(Å)	5.52291(3)	5.52519(5)	5.53024(9)
c(Å)	7.53471(4)	7.54501(7)	7.57100(9)
V(Å^3)	217.97(1)	218.78(1)	220.78(1)
R_{avg} (Å)	1.065	1.072	1.084
t	0.865	0.867	0.872
S	0.052964(1)	0.051421(1)	0.047591(1)
$Cr1$-$O1$-$Cr1$ (deg)	146.38	146.64	148.12

Cr1-O1 (Å)		1.968	1.975	1.968
Cr1-O2 (Å)		1.994	2.010	2.009
Cr1-O2 (Å)		1.986	1.966	1.974
Ho/R (4c)	x/a	-0.01812(21)	-0.01718(24)	-0.01684(27)
	y/b	0.06658(10)	0.06542(10)	0.06337(11)
	z/c	0.25000	0.25000	0.25000
Cr (4c)	x/a	0.50000	0.50000	0.50000
	y/b	0.00000	0.00000	0.00000
	z/c	0.00000	0.00000	0.00000
O1 (4c)	x/a	0.1018(98)	0.1040(95)	0.09591(113)
	y/b	0.4641(91)	0.4602(83)	0.4655(100)
	z/c	0.25000	0.25000	0.25000
O2 (4c)	x/a	-0.30735(77)	-0.30117(73)	-0.30272(88)
	y/b	0.30270(80)	0.30182(75)	0.30250(90)
	z/c	0.05388(52)	0.05501(50)	0.05237(59)
L (nm)		96(12)	104(13)	99(11)

SEM images elucidating the surface morphology of HTCO, HCO, and HGCO samples are shown in Fig. 2(a)-(c). No obvious impurity was found in these samples. A representative EDS spectrum of HTCO is shown in Fig. 2(d). The X-ray detector counts are quite high, yielding decent signal-to-noise ratios for the detection of O, Cr, Ho, and Tm.

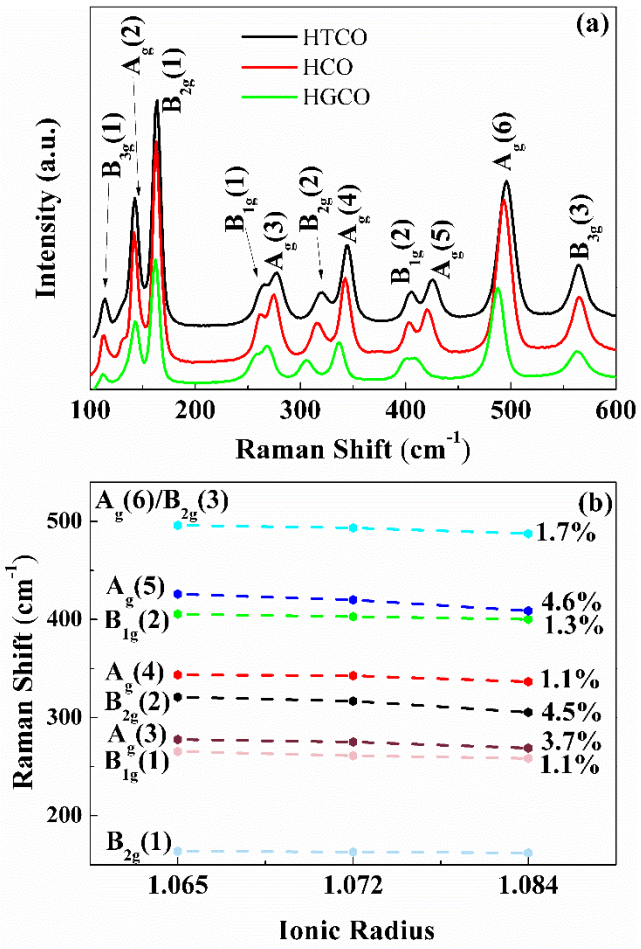

FIG. 3. (a) Raman spectra of $Ho_{0.67}Tm_{0.33}CrO_3$ (HTCO), $HoCrO_3$ (HCO), and $Ho_{0.67}Gd_{0.33}CrO_3$ (HGCO) samples. (b) Raman shift of phonon modes as a function of A-site ionic radius (R_{avg}) of HTCO, HCO and HGCO; The solid lines are visual guides connecting the data points with the number next to each line representing % decrease of the line positions with increase in $R_{avg.}$

In order to further examine the phase purity and structural characteristics of the samples, their Raman spectra measured at room temperature are shown in Fig. 3(a). The phonon Raman modes are labeled according to prior reports on $RCrO_3$ systems [40,41]. Among the 24 Raman active modes ($7A_g+5B_{1g}+7B_{2g}+5B_{3g}$) according to group theory, 12 modes within 100–600 cm^{-1} range for the orthorhombic *Pbnm* perovskite structure are present. The positions of the Raman modes of the three samples investigated here are compared in Table II and plotted in Fig. 3(b). For the $A_g(2)$ and $B_{2g}(1)$ modes, the line positions are essentially unchanged within experimental uncertainties for the three samples. These modes with line positions below 200 cm^{-1} are due to A-O vibrational frequencies involving the heavier A atoms (Tm, Ho, Gd). Since the change in A-site mass in going from HTCO to HGCO is about 2% and the frequency varies inversely as the square root of mass, the frequency shift expected from this effect is about 1 % assuming no change in the coupling constant. The position of all the other Raman modes shifts to lower

frequencies in going from the sample HTCO to HCO to HGCO for which R_{avg} increases in the same order of the samples. The maximum percentage decrease of the line shifts for the three samples from HTCO to HGCO, listed in Fig. 3(b), is as high as 4.6 % for the Ag(5) mode. This decrease of the frequency shifts with increasing R_{avg} is in good agreement with the report of Weber *et al.* [40] in which extensive discussion on the assignment of the various Raman modes is also provided. The important result from this discussion is that the R_{avg}–dependent shift is correlated with the main structural distortion of in-plane O-Cr-O bond angles and hence octahedral tilting [40]. The broadening of some Raman modes evident in Fig. 3(a) for the HTCO and HGCO samples as compared to those in the HCO sample may be due to the inhomogeneity of the atoms on the A-site due to doping.

Bhadram *et al.* [41] have investigated the temperature dependence of the Raman modes in a number of $RCrO_3$ systems and reported that anomalies in the linewidth of Raman modes around T_N is observed only if R^{3+} is a magnetic ion such as Gd^{3+}, signaling the presence of spin-coupling via the R^{3+}- Cr^{3+} exchange coupling. Since this R^{3+}- Cr^{3+} exchange coupling is weaker than the Cr^{3+}-Cr^{3+} exchange coupling, its effect on the Raman modes at room temperature is likely not observable.

Table II. Positions and assignment of the Raman modes in $Ho_{0.67}Tm_{0.33}CrO_3$ (HTCO), $HoCrO_3$ (HCO), and $Ho_{0.67}Gd_{0.33}CrO_3$ (HGCO) powder samples.

Sample	$A_g(2)$	$B_{2g}(1)$	$B_{1g}(1)$	$A_g(3)$	$B_{2g}(2)$	$A_g(4)$	$B_{1g}(2)$	$A_g(5)$	$A_g(6)$	$B_{3g}(3)$
$Ho_{0.67}Tm_{0.33}CrO_3$	142.58(21)	163.76(32)	265.41(26)	277.06(40)	319.28(36)	343.50(42)	405.48(44)	426.05(34)	495.95(28)	565.31(47)
$HoCrO_3$	141.79(30)	162.96(27)	261.13(15)	275.07(38)	315.02(29)	342.70(44)	402.97(51)	420.11(39)	493.45(41)	564.51(47)
$Ho_{0.67}Gd_{0.33}CrO_3$	142.57(34)	161.99(28)	258.44(30)	267.12(27)	305.41(35)	336.59(37)	400.33(41)	407.20(38)	487.46(46)	561.94(45)

3.2. Optical absorption

The optical absorbance of the samples was measured in the wavelength range of 200-800 nm and the results are presented in Figs. 4(a), 4(b), and 4(c). In $RCrO_3$, the energy states are composed of the R^{3+}-4f level, the filled O^{2-}- 2p band, the partially filled Cr^{3+}-3d, and the empty Cr^{3+}-4s band [13]. The peak at 455.5 nm results from the $^4A_2$ to $^4T_2$ transition, whereas the peak at around 610 nm is attributed to the $^4A_2$ to $^4T_1$ transition following the report of Gupta *et al.* [13]. Moreover, due to the high sensitivity of our system, peaks at around 300 nm, which were not reported by Gupta *et al.*, are interpreted by the 4f-5d and charge transfer transitions [13]. The overall shift between the peak positions may be explained by the difference of R_{avg}.

The optical absorption edge is related to the band energy, and the energy band gap (E_g) can be calculated by Tauc's equation [42, 43]

$$\alpha h\nu = A\left(h\nu - E_g\right)^n. \quad (1)$$

Here α is the optical absorption coefficient, $h\nu$ is the energy of the incident photon, A is a characteristic parameter, and n=1/2 (2) for direct (indirect) transitions. Based on this equation, Figs. 4(d), 4(e), and 4(f) show the plots of $(\alpha h\nu)^2$ vs. $h\nu$ for the three samples, and the linear absorption-edge curve was fitted with a straight line, the intersection of which with the $(\alpha h\nu)^2$=0 axis gives values of E_g as ~ 3.06, 3.14, and 2.75 eV, for HTCO, HCO, and HGCO bulk samples, respectively. Both Tm and Gd doping is found to lower the E_g of HCO sample. Clearly, E_g of HGCO sample is smaller than that of HCO sample but slightly larger than that of the $GdCrO_3$ sample (2.7 eV) [44], i.e. in between the two end members, corroborating the doping/substitution effect. Additionally, E_g of HCO sample is almost equal to the calculated value of 3.1 eV [16], but slightly smaller than that Kotnana *et al.* experimentally reported (3.26 eV) [15]. These results, along with E_g values of the other $RCrO_3$ compounds from the literature, are summarized in Table III. Thus, it can be clearly seen that the band gap of HCO may be simply tuned by A-site doping by various rare-earth ions, signifying its potential application as a photocatalyst.

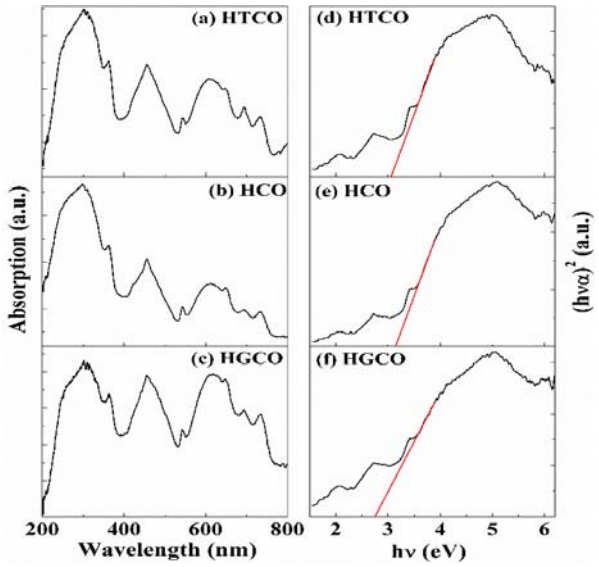

FIG. 4. Optical absorption spectra of (a) $Ho_{0.67}Tm_{0.33}CrO_3$ (HTCO), (b) $HoCrO_3$ (HCO), and (c) $Ho_{0.67}Gd_{0.33}CrO_3$ (HGCO) samples along with the respective (d-f) plots of $(\alpha h\nu)^2$ vs. $h\nu$ for the samples following Eq. (1) with the extrapolated red line determining the direct energy gap.

Table III. A comparison of the energy band gap (E_g) of some rare-earth chromites ($RCrO_3$) obtained experimentally (Ex) or theoretically (Th).

Sample	**$DyCrO_3$**		**$LaCrO_3$**		**$HoCrO_3$**		**$NdCrO_3$**	**$Ho_{0.67}Tm_{0.33}CrO_3$**	**$HoCrO_3$**	**$Ho_{0.67}Gd_{0.33}CrO_3$**	**$GdCrO_3$**
E_g (eV)	2.8	2.7	3.4		3.26	3.1	1.78	3.06(7)	3.14(6)	2.75(6)	2.7
Method	Ex	Th	Ex	Th	Ex	Th	Ex	Ex	Ex	Ex	Ex

Ref.	[13]	[16]	[45]	[46]	[15]	[16]	[47]	This work	[44]

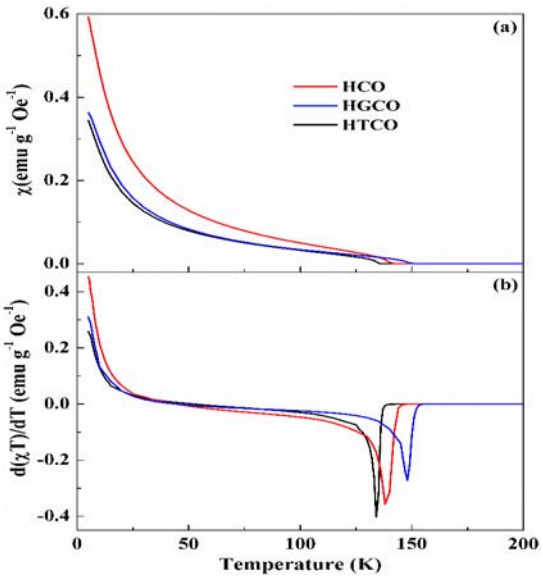

FIG. 5. (a) Temperature dependence of the magnetic susceptibility (χ) of $Ho_{0.67}Tm_{0.33}CrO_3$ (HTCO), $HoCrO_3$ (HCO), and $Ho_{0.67}Gd_{0.33}CrO_3$ (HGCO) measured in H = 50 Oe. (b) Plots of ($d(\chi T)/dT$) vs. T from 5 to 200 K to determine T_N^{Cr}, the ordering temperature of Cr^{3+} moments.

3.3. Magnetic properties:

Temperature dependence of the dc magnetic susceptibility ($\chi=M/H$) for the three samples measured at a magnetic field H=50 Oe (1 Oe=10^{-4} T) in field cooled (FC) modes is plotted in Fig. 5 (a). At 5 K, the magnitudes of χ are 0.344, 0.593, and 0.363 emu g^{-1} (emu g^{-1} = Am^2 kg^{-1}) for HTCO, HCO, and HGCO bulk samples, respectively. Their relative magnitudes can be explained by the differences in the magnetic moments (μ) of Ho^{3+} (10.4 μ_B), Tm^{3+} (7.57 μ_B), and Gd^{3+} (7.94 μ_B). As μ(Tm) < μ(Gd) < μ(Ho), HTCO and HCO samples show the smallest and largest χ, respectively. With increasing temperature, magnitudes of χ of the present samples decrease, and then drop rapidly to very low values at a characteristic temperature ~ 150 K, followed by a very slow decrease thereafter. This characteristic temperature is the ordering temperature of the Cr^{3+} ions, namely the Néel temperature (T_N^{Cr}). To accurately determine T_N^{Cr}, the temperature variation of χT data was utilized since in antiferromagnets near T_N, the temperature variation of $d(\chi T)/dT$ is similar to that of heat capacity [48]. Fig. 5(b) presents the temperature dependent $d(\chi T)/dT$ data, from the minimum of which T_N^{Cr} is determined to be 134 K, 139 K, and 148 K for HTCO, HCO, and HGCO bulk samples, respectively. These are consistent with the corresponding values reported for the end member compositions: 140 K, 125 K, and 167 K for $HoCrO_3$ [16], $TmCrO_3$ [35], and $GdCrO_3$ [26]. Importantly, these results show that T_N^{Cr} of HCO is lowered by doping at the A-site with Tm^{3+} (ionic radius smaller than that of Ho^{3+}) but increases by doping with Gd^{3+}

with ionic radius larger than that of Ho^{3+}. Interpretation of this important result is presented later in this paper.

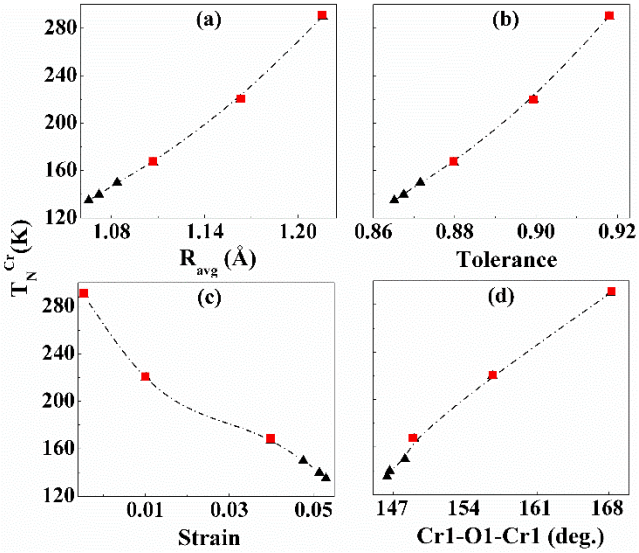

FIG. 6. The dependence of Néel temperature (T_N^{Cr}) on (a) average radii of A-site ions (R_{avg}), (b) tolerance factor (t), (c) orthorhombic strain, and (d) the in-plane Cr1-O1-Cr1 bond angle. The black triangles represent the data of $Ho_{0.67}Tm_{0.33}CrO_3$, $HoCrO_3$, and $Ho_{0.67}Gd_{0.33}CrO_3$ samples and the red squares represent the data of $GdCrO_3$, $NdCrO_3$, and $LaCrO_3$ taken from the literature [36, 40].

As mentioned above, the structural and magnetic properties of $RCrO_3$ are significantly dependent on R_{avg}, and T_N^{Cr} increases with an increasing R_{avg} [36]. To clearly demonstrate the dopant effect, the dependence of T_N^{Cr} on R_{avg}, the tolerance factor (t), orthorhombic strain (S), and the Cr1-O1-Cr1 bond angles are plotted in Fig. 6 in which the black triangles represent the data of our samples of HTCO, HCO and HGCO and the red squares represent the data of $GdCrO_3$, $NdCrO_3$, and $LaCrO_3$ taken from the literature [36, 40]. It is evident that T_N^{Cr} increases almost linearly with the increasing value of R_{avg}, t, and the Cr1-O1-Cr1 bond angle, but decreases with the increase in the value of S. Thus, it can be inferred that the T_N^{Cr} of $RCrO_3$ compounds is related to distortions in the crystal structure and can be tuned by appropriate rare-earth doping.

Next, the effect of hydrostatic pressure on the Neel temperature of HCO bulk sample was investigated by measuring the relative temperature-dependence of mutual inductance under

different hydrostatic pressures (0-16.5 kbar). When the magnetization of the sample changes, an anomaly in the mutual inductance of secondary coil is observed. As shown in Fig. 7 (a), the sharp increase in the slope of the curve results from the magnetic ordering of Cr^{3+} ions with T_N^{Cr} determined by the peak position. As shown in Fig. 7(b), T_N^{Cr} increases with increasing pressure, which agrees well with the results of $RCrO_3$ obtained theoretically [33]. Similarly, Poudel *et al*. reported that the Néel temperature of multiferroic $GdMn_2O_5$ single crystal increases with increasing hydrostatic pressure [49]. In addition, Alonso *et al*. observed that the external pressure induces structural changes in $RMnO_3$ samples, yielding larger Mn-O-Mn bond angles and tolerance factors [50]. Therefore, the application of external pressure in $HoCrO_3$ plays a similar role qualitatively as introducing a larger-radius dopant like Gd in the present case.

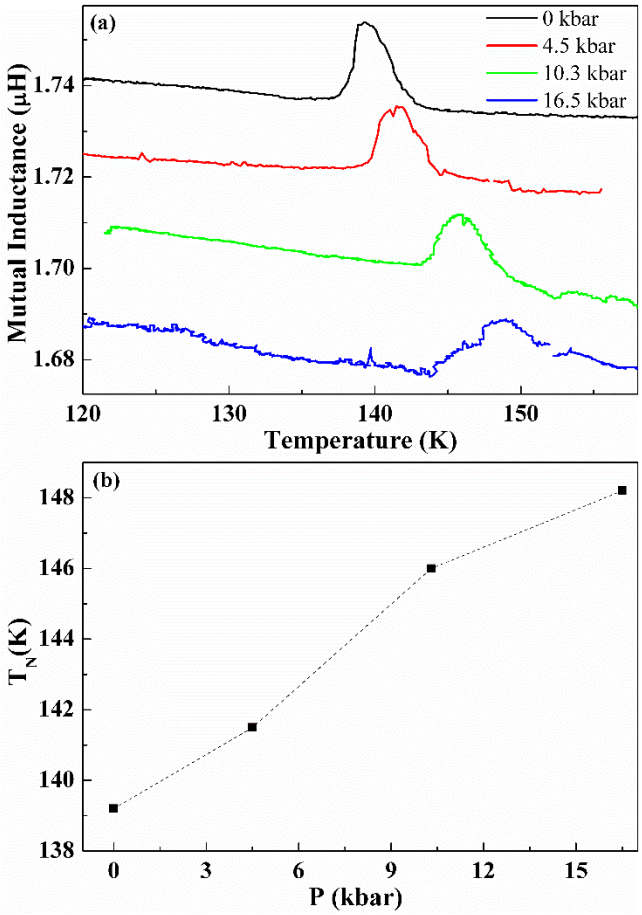

FIG. 7. (a) The temperature dependence of mutual inductance of $HoCrO_3$ pellet sample under different hydrostatic pressure (0-16.5 kbar), (b) Néel temperature (T_N^{Cr}) of $HoCrO_3$ sample as a function of the hydrostatic pressure. The line joining the points in (b) is drawn for visual clarity.

A quantitative interpretation of the temperature dependence of the magnetic susceptibility above the Neel temperature T_N^{Cr} due to the ordering of Cr^{3+} ions is presented next by first fitting the data to the Curie-Weiss (CW) law: $\chi=C/(T-\theta)$ (C is the Curie constant, θ is the Weiss

temperature). The temperature dependent $1/\chi$ data and the CW fittings are shown in Figs. 8(a), 8(b), and 8(c). With the fitted C value, the effective magnetic moment was then calculated suing Equation 2:

$$\mu_{eff} = \sqrt{\frac{3k_B C}{N}}, \tag{2}$$

where k_B is the Boltzmann constant and $N = N_A/MW$ is the number of magnetic ions per gram of the sample determined from the Avogadro's constant N_A and molecular weight (MW) of the sample [51]. Alternatively, the effective magnetic moment $\mu_{eff}{}^a$ can be calculated using the free ionic moments of Ho^{3+}, Tm^{3+}, Gd^{3+}, and Cr^{3+} (3.8 μ_B) [16].

$$\mu_{eff}{}^a = \sqrt{\mu_{Cr}^2 + (1-x)\mu_{Ho}^2 + x\mu_{Gd,Tm}^2}, \tag{3}$$

Magnitudes of all these parameters (T_N^{Cr}, C, θ, μ_{eff}, and $\mu_{eff}{}^a$) determined from the above analysis are summarized in Table IV. The excellent agreement between μ_{eff} and $\mu_{eff}{}^a$ values found for all compositions confirms the correctness of the employed procedures and the chemical composition and phase purity of the samples used in the calculations.

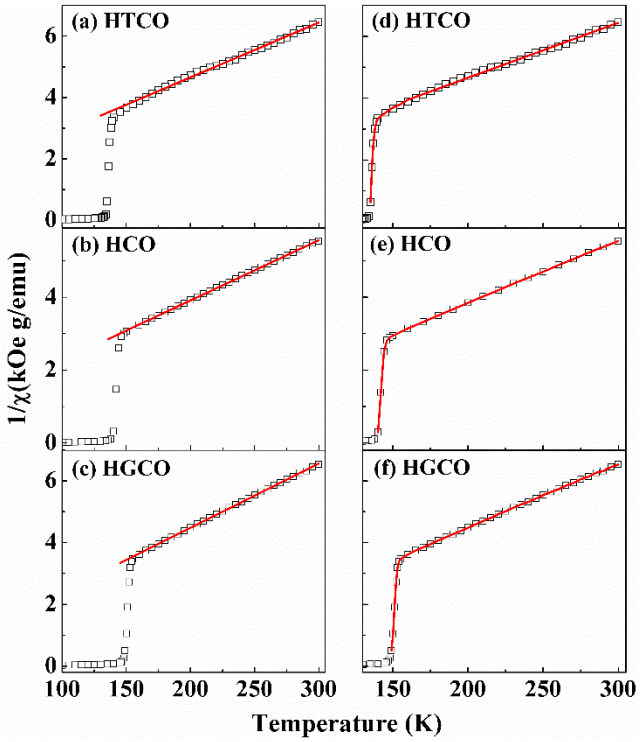

FIG. 8. Temperature dependence of inverse susceptibility ($1/\chi$) of (a) $Ho_{0.67}Tm_{0.33}CrO_3$ (HTCO), (b) $HoCrO_3$ (HCO), and (c) $Ho_{0.67}Gd_{0.33}CrO_3$ (HGCO) samples with the black squares as data

points and the red solid line fits to the Curie–Weiss law. In (d), (e) and (f), the red lines are the corresponding fits to the modified Curie–Weiss law of Eq. (4) that includes the DM interaction.

From Figs 8(a), 8(b), and 8(c) it is evident that the CW fitting works well in the high temperature regime well above T_N^{Cr}, but fails near or below T_N^{Cr}. This is because the present samples exhibit weak ferromagnetism below T_N^{Cr} and are canted antiferromagnets instead of simple antiferromagnets. This weak ferromagnetism is due to the Dzyaloshinskii-Moriya (DM) antisymmetric exchange interaction whose effect was included by Moriya on the temperature dependence of the paramagnetic susceptibility using a molecular field approximation [52]. According to this theory, the susceptibility in the easy-axis direction obeys the Curie-Weiss law, whereas the susceptibility perpendicular to the easy-axis also depends on the DM interaction. Since the susceptibility in the direction parallel and perpendicular to the easy-axis could not be measured separately for the present polycrystalline samples, we use the equations for the dominant contribution from the perpendicular direction, as modeled by Moriya [52]:

$$\chi = \frac{C\prime}{(T-\theta\prime)}\frac{T-T_0}{(T-T_N^{Cr\prime})}, \tag{4}$$

where T is the temperature, T_0 and $T_N^{Cr\prime}$ are fitting parameter, given by [52]:

$$T_0 = \frac{2J_eZS(S+1)}{3k_B}, \tag{5}$$

$$T_N^{Cr\prime} = \frac{2J_eZS(S+1)}{3k_B}\left[1+\left(\frac{D}{2J_e}\right)^2\right]^{\frac{1}{2}}. \tag{6}$$

Here $Z = 6$ is the coordination number of Cr^{3+} relative to other Cr^{3+} ions and S=3/2 is the spin quantum number of Cr^{3+}. Eqs. (5) and (6) give semi-quantitative analyses of J_e and D, the magnitudes of the symmetric and antisymmetric Cr^{3+}-Cr^{3+} exchange interactions, respectively. The Cr^{3+}-Cr^{3+} exchange interactions can be extracted from the above parameters, as T_N^{Cr} is far above the rare-earth ordering temperature where other exchange interactions (R^{3+}-R^{3+} and R^{3+}-Cr^{3+}) are ignorable. In Figs. 8(d), 8(e), and 8(f), the plots of $1/\chi$ vs. T data for the three samples approaching T_N^{Cr} for $T > T_N^{Cr}$, along with the fits to Eq. (4) are shown. Note that the magnetization data were measured in an interval of 0.5 K near T_N^{Cr} in order to provide a better test for the model. All the fitted parameters listed in Table IV, such as Curie constant (C'), T_0, Weiss temperature (θ'), and temperature ($T_N^{Cr\prime}$) are close to those obtained using a CW fit and $d(\chi T)/dT$ vs. T plot.

The above analysis shows that the exchange constant J_e/k_B = 8.96 K, 9.44 K and 10.02 K determined respectively for the three samples of HTCO, HCO and HGCO discussed here increases in the same order as the *Cr1-O1-Cr1* bond angles listed in Table 1 for these samples. This is understandable since the Cr-Cr superexchange coupling depends on this bond angle as

well as *Cr1-O1* bond lengths. This correlation between the structural properties and magnetic properties is considered to be an important result of this work.

An interpretation of the observed increase in T_N^{Cr} of HCO with increase in applied hydrostatic pressure shown in Fig. 7 is considered next. Using Raman spectroscopy as a probe, Bhadram *et al.* [31] have reported on the changes in the octahedral distortions under hydrostatic pressure in several $RCrO_3$ systems (R = Lu, Tb, Gd, Eu, Sm). These octahedral distortions with increase in hydrostatic pressure result in changes in the *Cr1-O1-Cr1* bond angle and *Cr1-O1* bond lengths which in turn affects the exchange coupling and hence the measured T_N^{Cr}. Their main conclusion from these investigations was that pressure dependence of T_N^{Cr} in $RCrO_3$ (R= Gd, Eu, Sm) is largely due to due to the compression of the Cr1-O1 bonds rather than changes in the *Cr1-O1-Cr1* bond angle. Extending this argument to the three samples investigated here, it would appear that the results of the changes in T_N^{Cr} with chemical doping and hydrostatic pressure have slightly different origins, the former dominated by changes in the *Cr1-O1-Cr1* bond angle and the latter dominated by and *Cr1-O1* bond lengths. The calculation of super-exchange constant from first principles is usually quite difficult since it requires exact knowledge of the wave-functions involved. However, semi-quantitative determination of changes in J_e under hydrostatic pressure and chemical doping might be possible using modern DFT (density functional theory) codes.

Table IV. The magnetic parameters: Cr^{3+} ordering temperature T_N^{Cr} (K), the Weiss temperature θ (K), Curie constant C (emu K Oe^{-1} mol^{-1}), and effective magnetic moment μ_{eff} (μ_B) obtained by Curie-Weiss fit of the susceptibility data; the $T_N^{Cr\prime}$(K), θ′(K), C′ (emu K Oe^{-1} mol^{-1}), the fitting parameter T_0 (K), the symmetric exchange constant J_e (K), and the antisymmetric exchange constant D_e resulting from the modified Curie-Weiss fitting the dc susceptibility data. μ_{eff} [a] is calculated by free ionic moments of Cr^{3+} and Ho^{3+} ions.

samples	$Ho_{0.67}Tm_{0.33}CrO_3$	$HoCrO_3$	$Ho_{0.67}Gd_{0.33}CrO_3$
T_N^{Cr}(K)	135.0(1)	139.2(2)	148.5(1)
C (emu K Oe^{-1} mol^{-1})	13.07(5)	17.01(4)	13.10(4)
θ (K)	-27.68(81)	-36.47(60)	-15.48(77)
μ_{eff} (μ_B)	10.22(2)	11.66 (1)	10.23(2)
μ_{eff} [a] (μ_B)	10.29	11.23	10.63
$T_N^{Cr\prime}$ (K)	135.2 (1)	139.9(2)	149.7(4)
T_0 (K)	134.4 (2)	141.7(2)	150.4(1)
J_e/k_B (K)	8.96(1)	9.44 (1)	10.02 (1)

D/k_B (K)	1.92 (3)	1.23(6)	1.41(2)
θ' (K)	-80.3(4)	-29.1(5)	-25.2(3)
C' (emu K Oe^{-1} mol^{-1})	15.73(2)	17.01(4)	13.10(4)
μ'_{eff} (μ_B)	10.62(8)	11.21(10)	10.20(6)

To investigate the dependence of magnetization (M) on magnetic field (H), isothermal M–H curves were measured between 5 and 145 K for the three samples and these results are shown in Fig. 9(a)-(c). At T = 5 K and H = 40 kOe (4 Tesla), magnetization values for HTCO, HCO, and HGCO bulk samples are 69.3, 86.0, and 96.3 emu g^{-1}, respectively. Clearly, the magnitude of M decreases with Tm doping but it increases with Gd doping. These changes in the magnitudes of M on chemical doping correlate well with the observed changes in T_N^{Cr} which in turn depend on the changes in the *Cr1-O1-Cr1* bond angle. Note that in Table I, the observed changes in the *Cr1-O1-Cr1* bond angle on Gd doping are much larger than those observed with Tm doping, similar to the observed changes in the magnetic parameters for these systems (Table IV).

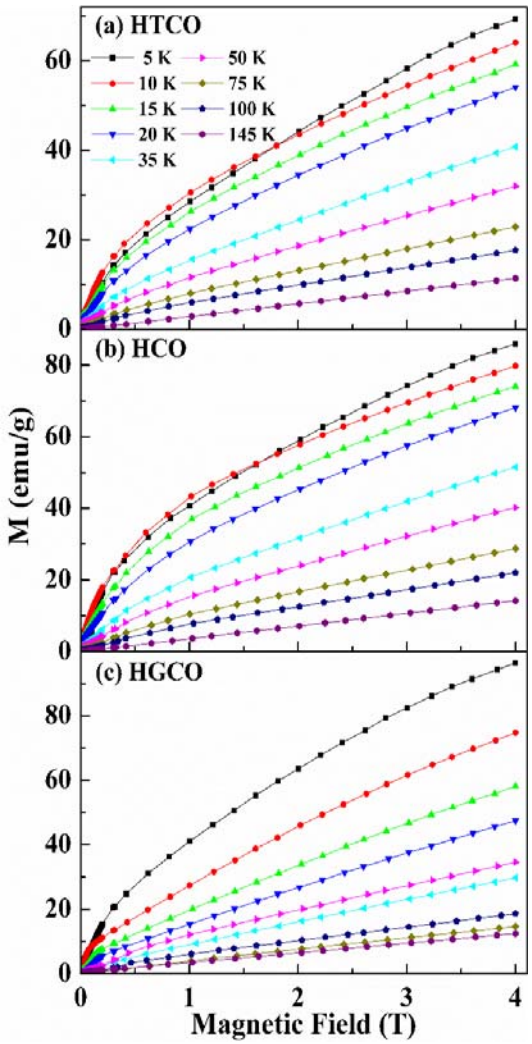

FIG. 9. Isothermal magnetization curves vs. applied magnetic field (in first quadrant) at select temperatures between 5 K and 145 K for (a) $Ho_{0.67}Tm_{0.33}CrO_3$ (HTCO), (b) $HoCrO_3$ (HCO), and (c) $Ho_{0.67}Gd_{0.33}CrO_3$ (HGCO) samples. The lines joining the data points are visual guides.

The measured *M–H* curves at lower temperatures in Fig. 9 are not linear. This low-temperature non-linearity is due to the presence of a weak ferromagnetic component resulting from the canting of the Cr^{3+} moments whereas the linear component is due to paramagnetism of Ho^{3+} ions (above its ordering temperature) and the underlying antiferromagnetism of Cr^{3+} ions. With increase in temperature from 5 K, the weak ferromagnetic component decreases in strength as expected, and *M–H* curves becomes increasingly linear as evident at T =145 K for HCO sample due to the presence of paramagnetism of Cr^{3+} ions above T_N^{Cr}.

3.4. Magneto-caloric properties:

The isothermal *M* vs. *H* data presented in Fig. 9 is used next to determine the magneto-caloric properties of the present samples that can be defined in terms of the three parameters. The first is the magnetic entropy change (ΔS), which can be derived from the Maxwell relation [53]:

$$\Delta S(T,H) = \int_0^H \left(\frac{\partial M(T,H)}{\partial T}\right)_H dH \approx \sum_i \frac{M_{i+1}(T_{i+1},H) - M_i(T_i,H)}{T_{i+1} - T_i} \Delta H \quad (7)$$

Since the magnetization is measured in discrete field and temperature intervals, ΔS can be approximately calculated by the summation from the isothermal *M* vs. *H* curve in Fig. 9. The second parameter is the refrigeration capacity (*RC*), which is the amount of heat transfer between the cold and hot reservoirs in a magnetic refrigerator and defined by Equation 8:

$$RC = -\int_{T_1}^{T_2} |\Delta S_{M,H}| dT \quad (8)$$

where T_1 and T_2 are the temperature of the cold and hot reservoirs, respectively. The refrigeration efficiency of a material is mainly dependent on *RC*. The third parameter is the adiabatic temperature change (ΔT_{ad}), calculated using Equation 9 [54]:

$$\Delta T_{ad} = \mu_0 \int_0^H \frac{T}{C_H} \left(\frac{\partial M}{\partial T}\right)_H dH \approx \frac{T}{C_P} \Delta S \quad (9)$$

The above approximation was based on the precondition that T/C_H shows little dependence on the magnetic field as reported by Su *et al.* [55]. The maximum ΔT_{ad} is calculated using $C_H/T \approx 0.8$ J/(mol K^2) at ~20 K for HCO.

In Fig. 10(a), the representative thermal variation of ΔS of HTCO sample at various applied fields (H=1 to 7 T) is presented. It is evident that at a given temperature, magnitudes of ΔS increase with increase in magnetic field since a larger magnetic field induces a larger magnetization thus leading to larger ΔS (see Eq. 7). With increase in temperature from 5 K,

magnitude of ΔS of HTCO first increases, reaching a maximum at ~17 K and decreases thereafter. The maximum magnitude of ΔS of HTCO obtained is 6.7 J/kg K at 17 K and at H=7 T. For comparison, ΔS ~4.6 J/kg K at H=5 T and T=10-20 K for the pure $TmCrO_3$ powder sample was reported [35] which is similar to $\Delta S \sim 4.5$ J/kg K under 5 T and 17 K for HTCO sample.

Fig. 10(b) shows the RC value of the present HTCO sample (T_1 = 5 K and T_2 = 100 K). Like ΔS, the RC value also increases with increasing magnetic field from 1 T to 7 T. At 7 T, the RC value of the present HTCO sample is 295.3 J/kg, compared to 86 J/kg for $TmCrO_3$ sample under H=5 T (T_1=5 K and T_2=25 K) [35].

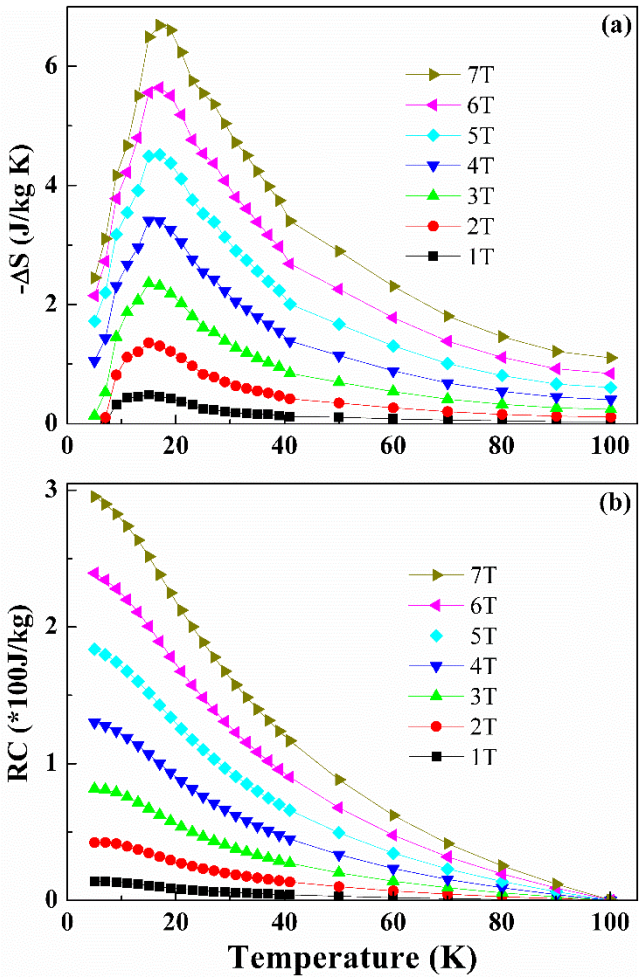

FIG. 10. The temperature dependence of (a) entropy change (ΔS) and (b) refrigeration capacity (RC) of $Ho_{0.67}Tm_{0.33}CrO_3$ (HTCO) sample in magnetic fields up to 7T (70 kOe).

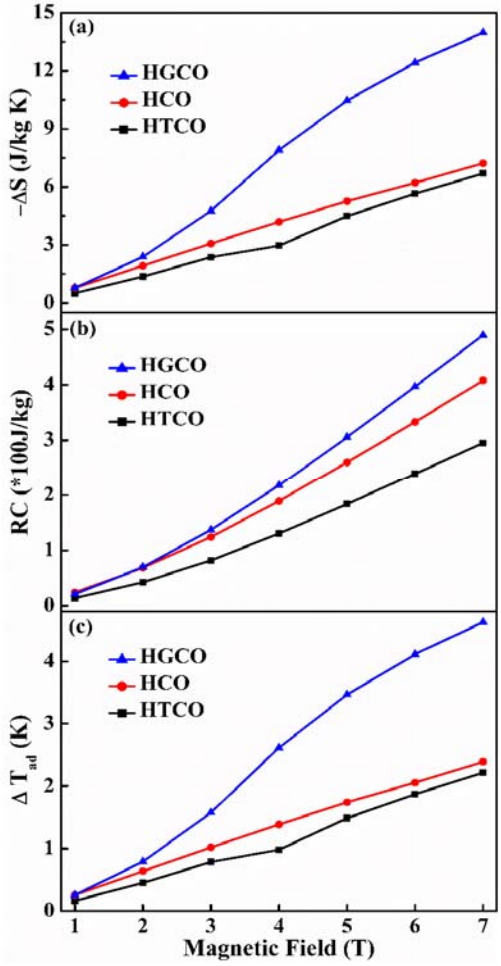

FIG. 11. (a) The maximum of magnetic entropy change (-Δ*S*), (b) refrigeration capacity (*RC*), and (c) adiabatic temperature change (ΔT_{ad}) as a function of magnetic field for $Ho_{0.67}Tm_{0.33}CrO_3$ (HTCO), $HoCrO_3$ (HCO), and $Ho_{0.67}Gd_{0.33}CrO_3$ (HGCO) samples.

To compare the magneto-caloric characteristics of the three samples investigated here, the magnetic field dependence of Δ*S*, *RC*, and ΔT_{ad} for the three samples is presented in Fig. 11. Note that the magnitudes of these quantities for each sample increase with increasing applied magnetic field. As such, the nature of their field dependence is very similar, although the specific values differ. Notably, magnitudes of Δ*S*, *RC*, and ΔT_{ad} of the HCO sample are larger than those of HTCO, but smaller than those of HGCO. Hence, Tm doping was found to lower the magneto-caloric properties of HCO, whereas Gd doping was found to improve these properties. This trend follows the changes in the isothermal magnetization observed in Fig.9 on doping HCO with Tm and Gd, suggesting that the magnitude of the magnetization may be the controlling factor. For comparison, the magnetization of $GdCrO_3$ and HGCO at 5 K and 4 T are 105 emu/g [56] and 87 emu/g (Fig.9) respectively. Similarly, for the three samples of HTCO, HCO and HGCO, the MCE properties shown in Fig. 11 qualitatively scale with the M vs. H variations observed in Fig.

9. The large MCE observed in $GdCrO_3$ has been suggested to result from the large Gd^{3+}-Gd^{3+} magnetic interaction although no quantitative analysis in this regard was presented [56].

The dopant effect on MCE is likely not related to R_{avg}, since McDannald *et al*. doped $DyCrO_3$ powder samples on the A-site with Y, Er, and Ho, all of which have smaller R_{avg} than Dy. In that case, Y and Ho doping lowered MCE, whereas Er doping improved MCE [25]. Most likely, the enhancement in MCE by Gd doping in $HoCrO_3$ in the present study is related to the reported giant MCE of $GdCrO_3$ for which the magnitude of ΔS is 27 J/kg K at 5 K and 4.4 T [56], compared to the magnitude of ΔS of about 10 J/ kg K for HGCO under the same (H,T) conditions. In any case, the observed improvement of the MCE in $HoCrO_3$ by Gd doping at the A-site is very encouraging and holds promise for further tuning of the MCE by optimizing the A site dopant (both nature and content) in $RCrO_3$ compounds for their potential applications in magnetic refrigeration in low-temperature region.

4. Conclusions

In this work, we report on the changes in structural, optical, magnetic and magneto-caloric properties of $HoCrO_3$ powder sample arising from doping at the A-site (chemical pressure) with two different ions having ionic radii smaller (Tm^{3+}) and larger (Gd^{3+}) than Ho^{3+}. Three compositions studied in this work $Ho_{0.67}Tm_{0.33}CrO_3$ (HTCO), $HoCrO_3$ (HCO), and $Ho_{0.67}Gd_{0.33}CrO_3$ (HGCO) prepared by citrate route were found to crystallize in the orthorhombically distorted perovskites structure (space group of *Pbnm*). Analyses of the optical absorption spectra show direct band gaps E_g=3.06 eV, 3.14 eV, and 2.75 eV for HTCO, HCO, and HGCO, respectively. The ordering temperature of Cr^{3+}, T_N^{Cr} was determined from the temperature dependence of magnetic susceptibility data and was found to be 139 K for HCO, which is decreased to 135 K for HTCO, but increased to 148 K for HGCO sample. These changes are related to R_{avg}, the tolerance factor, the Cr1-O1-Cr1 bond angle, and the orthorhombic strain factor although it is argued that the Cr1-O1-Cr1 bond angle which affects the Cr^{3+}-Cr^{3+} superexchange interaction is the likely controlling factor. The observed increase in T_N^{Cr} of HCO with the applied hydrostatic pressure up to 16.5 kbar is qualitatively similar to doping with larger Gd^{3+} ion (chemical pressure) for Ho^{3+} ion at the A-site. However it is argued that the results of the changes in T_N^{Cr} with chemical doping and hydrostatic pressure have slightly different origins, the former dominated by changes in the *Cr1-O1-Cr1* bond angle and the latter dominated by changes in *Cr1-O1* bond lengths. Fitting of the temperature dependence of the paramagnetic susceptibility to the modified Curie-Weiss law including the Dzyloshinsky-Moriya (DM) interaction is used to determine the effect of Tm or Gd doping on T_N^{Cr}, the exchange constant J_e, and the DM interaction. The magnetic field dependent magnetization data (up to 7 T field) are used to determine the magneto-caloric properties of these samples. At H =7 T, the maximum magneto-caloric entropy changes for HTCO, HCO and HGCO are 6.69 J/kg K,

7.22 J/kg K, and 14.0 J/kg K, and their refrigeration capacities are 295 J/kg, 408 J/kg, and 490 J/kg, respectively. The large magneto-caloric entropy change observed in $HoCrO_3$ and its tunability by Tm and Gd doping makes $HoCrO_3$ a promising system for next-generation low–temperature magnetic refrigeration. Based on this encouraging result, further enhancement in MCE properties may be possible by optimizing the A-site dopant or by increasing the Gd/Ho ratio.

Acknowledgments

This work was supported in part by a research grant from the U.S. National Science Foundation (grant # DMR-1310149). For the optical measurements, SLS acknowledges support of the US Department of Energy, Office of Basic Energy Sciences, Division of Chemical, Biological and Geological Sciences under grant DE-FG02-86ER13622.A000. Pressure dependent work at Houston was supported by the US Air Force Office of Scientific Research, the T.L.L. Temple Foundation, the J.J. and R. Moores Endowment, and the State of Texas through the Texas Center for Superconductivity.

References

[1] S.-W. Cheong and M. Mostovoy, Nat. Mater. 6, 13 (2007).

[2] G. Lawes and G. Srinivasan, J. Phys. D. Appl. Phys. 44, 243001 (2011).

[3] J. F. Scott, NPG Asia Mater. 5, e72 (2013).

[4] M. Mostovoy, Nat. Mater. 9, 188 (2010).

[5] J. R. Sahu, C. R. Serrao, N. Ray, U. V. Waghmare, and C. N. R. Rao, J. Mater. Chem. 17, 42 (2007).

[6] Z. X. Cheng, X. L. Wang, S. X. Dou, H. Kimura, and K. Ozawa, J. Appl. Phys. 107, 09D905 (2010).

[7] M. K. Sharma, T. Basu, K. Mukherjee, and E. V Sampathkumaran, J. Phys. Condens. Matter 28, 426003 (2016).

[8] S. Yin, T. Sauyet, M. S. Seehra, and M. Jain, J. Appl. Phys. 121, 063902 (2017).

[9] B. Rajeswaran, D. I. Khomskii, A. K. Zvezdin, C. N. R. Rao, and A. Sundaresan, Phys. Rev. B 86, 214409 (2012).

[10] B. Rajeswaran, P. Mandal, R. Saha, E. Suard, A. Sundaresan, and C. N. R. Rao, Chem. Mater. 24, 3591 (2012).

[11] A. Ghosh, A. Pal, K. Dey, S. Majumdar, and S. Giri, J. Mater. Chem. C 3, 4162 (2015).

[12] A. Ghosh, K. Dey, M. Chakraborty, S. Majumdar, and S. Giri, Europhys. Lett. 107, 47012 (2014).

[13] P. Gupta and P. Poddar, RSC Adv. 5, 10094 (2015).

[14] A. Jaiswal, R. Das, K. Vivekanand, T. Maity, P. M. Abraham, S. Adyanthaya, and P. Poddar, J. Appl. Phys. 107, 013912 (2010).

[15] G. Kotnana and S. N. Jammalamadaka, J. Appl. Phys. 118, 124101 (2015).

[16] S. Yin, V. Sharma, A. Mcdannald, F. A. Reboredo, and M. Jain, RSC Adv. 6, 9475 (2016).

[17] J. Beckers and G. Rothenberg, ChemPhysChem 6, 223 (2005).

[18] A. L. Linsebigler, G. Lu, and J. T. Yates, Chem. Rev. 95, 735 (1995).

[19] Z. Shao, W. Zhou, and Z. Zhu, Prog. Mater. Sci. 57, 804 (2012).

[20] S. C. Singhal, Solid State Ionics 135, 305 (2000).

[21] N. Russo, D. Mescia, D. Fino, G. Saracco, and V. Specchia, Ind. Eng. Chem. Res. 46, 4226 (2007).

[22] M. Siemons and U. Simon, Sensors and Actuators B. 126, 181 (2007).

[23] A. McDannald, L. Kuna, and M. Jain, J. Appl. Phys. 114, 113904 (2013).

[24] L. H. Yin, J. Yang, R. R. Zhang, J. M. Dai, W. H. Song, and Y. P. Sun, Appl. Phys. Lett. 104, 032904 (2014).

[25] A. McDannald and M. Jain, J. Appl. Phys. 118, 043904 (2015).

[26] S. Yin and M. Jain, J. Appl. Phys. 120, 043906 (2016).

[27] N. D. Todorov, M. V. Abrashev, V. G. Ivanov, G. G. Tsutsumanova, V. Marinova, Y. Q. Wang, and M. N. Iliev, Phys. Rev. B 83, 224303 (2011).

[28] V. Sharma, A. McDannald, M. Staruch, R. Ramprasad, and M. Jain, Appl. Phys. Lett. 107, 012901 (2015).

[29] K. Yamauchi, F. Freimuth, S. Blügel, and S. Picozzi, Phys. Rev. B 78, 014403 (2008).

[30] J. M. Chen, J. M. Lee, T. L. Chou, S. A. Chen, S. W. Huang, H. T. Jeng, K. T. Lu, T. H. Chen, Y. C. Liang, S. W. Chen, W. T. Chuang, H.-S. Sheu, N. Hiraoka, H. Ishii, K. D. Tsuei, E. Huang, C. M. Lin, and T. J. Yang, J. Chem. Phys. 133, 154510 (2010).

[31] V. S. Bhadram, D. Swain, R. Dhanya, M. Polentarutti, A. Sundaresan, and C. Narayana, Mater. Res. Express 1, 026111 (2014).

[32] H. J. Zhao, W. Ren, Y. Yang, X. M. Chen, and L. Bellaiche, J. Phys. Condens. Matter 25, 466002 (2013).

[33] H. J. Zhao, W. Ren, X. M. Chen, and L. Bellaiche, J. Phys. Condens. Matter 25, 385604 (2013).

[34] C. W. Chu and L. R. Testardi, Phys. Rev. Lett. 32, 766 (1974).

[35] K. Yoshii, Mater. Res. Bull. 47, 3243 (2012).

[36] J. Prado-Gonjal, R. Schmidt, J. J. Romero, D. Ávila, U. Amador, and E. Morán, Inorg. Chem. 52, 313 (2013).

[37] A. L. Patterson, Phys. Rev. 56, 978 (1939).

[38] P. Dutta, M. S. Seehra, S. Thota, and J. Kumar, J. Phys. Condens. Matter 20, 015218 (2008).

[39] M. Wojdyr, J. Appl. Cryst. 43, 1126 (2010).

[40] M. C. Weber, J. Kreisel, P. A. Thomas, M. Newton, K. Sardar, and R. I. Walton, Phys. Rev. B 85, 054303 (2012).

[41] V. S. Bhadram, B. Rajeswaran, A. Sundaresan, and C. Narayana, Europhys. Lett. 101, 17008 (2013).

[42] J. Tauc, Mater. Res. Bull. 3, 37 (1968).

[43] W. Kou and M. Seehra, Phys. Rev. B 18, 7062 (1978).

[44] K. M. Parida, A. Nashim, and S. K. Mahanta, Dalton Trans. 40, 12839 (2011).

[45] T. Arima, Y. Tokura, and J. B. Torrance, Phys. Rev. B 48, 17006 (1993).

[46] K. P. Ong, P. Blaha, and P. Wu, Phys. Rev. B 77, 073102 (2008).

[47] S. Saha, S. Chanda, A. Dutta, and T. P. Sinha, J. Sol-Gel Sci. Technol. 69, 553 (2014).

[48] A. McDannald, L. Kuna, M. S. Seehra, and M. Jain, Phys. Rev. B 91, 224415 (2015).

[49] N. Poudel, M. Gooch, B. Lorenz, C. W. Chu, J. W. Kim, and S. W. Cheong, Phys. Rev. B 92, 144430 (2015).

[50] J. A. Alonso, M. J. Martínez-Lope, and M. T. Casais, Inorg. Chem. 2000, 39, 917 (2000).

[51] J. M. D. Coey, Magnetism and Magnetic Materials (Cambridge University Press, Cambridge, 2009).

[52] T. Moriya, Phys. Rev. 120, 91 (1960).

[53] M. H. Phan and S. C. Yu, J. Magn. Magn. Mater. 308, 325 (2007).

[54] V. K. Pecharsky and K. A. Gschneidner, J. Appl. Phys. 86, 565 (1999).

[55] Y. Su, J. Zhang, Z. Feng, Z. Li, Y. Shen, and S. Cao, J. Rare Earths 29, 1060 (2011).

[56] L. H. Yin, J. Yang, X. C. Kan, W. H. Song, J. M. Dai, and Y. P. Sun, J. Appl. Phys. 117, 133901 (2015).